Urban Impervious Surface Extraction Using Seasonal Time Series SAR Images

Wenfu Wu, Zhenfeng Shao, Jiahua Teng, Xiao Huang, Xinwei Zhao, and Songjing Guo

***Abstract*—Urban impervious surface (UIS) is an essential indicator to measure urban ecology, and understanding its temporal and spatial distribution is of great significance for alleviating urban diseases, such as heat island. Although remote sensing techniques have been widely used to extract UIS, the capability of synthetic aperture radar (SAR) technology in UIS extraction has not been thoroughly investigated. Accordingly, this article systematically analyzed the role of the backscattering and interferometric coherence features of dual polarized (VH/VV) SAR in UIS extraction, taking Tianjin city, China, as a study case. Specifically, we used seasonal time series Sentinel-1B backscattering and coherence images to extract UIS via two object-based classifiers. We further investigated the seasonal, polarization, and precipitation effects on UIS extraction using SAR images. Our findings suggested that, for coherence images, the extraction accuracy of UIS in summer is the highest, while for backscattering that in spring and winter are the highest. Our results also suggested that VH polarization is more suitable for UIS extraction compared with VV polarization. These findings of this study confirmed the utility and effectiveness of time series SAR backscattering and coherence images in UIS extraction, providing an essential reference for UIS extraction in other places with a similar climate. We encourage more efforts to be made toward UIS extraction using SAR images and toward designing a filling scheme for the UIS extraction in a continuous manner, especially in cloudy and rainy areas.**

***Index Terms*—Coherence images, synthetic aperture radar (SAR) backscattering, seasonal effect, time series SAR images, urban impervious surface (UIS).**

Manuscript received 8 May 2022; revised 8 July 2022; accepted 19 July 2022. Date of publication 29 July 2022; date of current version 3 August 2022. This work was supported in part by the National Natural Science Foundation of China under Grant 42090012, in part by the Special Fund of Hubei Luojia Laboratory (220100009), in part by the 03 special research and 5G project of Jiangxi Province in China (20212ABC03A09), in part by the Zhuhai industry university research cooperation project of China (ZH22017001210098PWC), in part by the Key R & D project of Sichuan Science and technology plan (2022YFN0031), in part by the Zhizhuo Research Fund on Spatial-Temporal Artificial Intelligence (ZZJJ202202). *(Corresponding author: Jiahua Teng.)*

Wenfu Wu and Zhenfeng Shao are with the School of Remote Sensing and Information Engineering, Wuhan University, Wuhan 430079, China (e-mail: wuwwf09140818@whu.edu.cn; shaozhenfeng@whu.edu.cn).

Jiahua Teng is with the Satellite Environment Protetion Key Laboratory of Satellite Romote Sensing, Ministry of Ecology and Environment, Beijing 100094, China (e-mail: tengjh@secmep.cn).

Xiao Huang is with the Department of Geosciences, University of Arkansas, Fayetteville, AR 72701 USA (e-mail: xh010@uark.edu).

Xinwei Zhao is with the China Centre For Resources Satellite Data and Application, Beijing 100094, China (e-mail: zhaoxinwei@chinasiwei.com).

Songjing Guo is with the Institute of Geophysics and Geomatics, China University of Geosciences, Wuhan 430074, China (e-mail: guosongjing@cug.edu.cn).

Digital Object Identifier 10.1109/JSTARS.2022.3193137

I. Introduction

CHINA has experienced rapid urbanization in the past 40 years since the implementation of the reform and opening-up policy in 1978 [1]. In 2021, the urbanization rate of China has reached 63.89% and is expected to reach 75%–80% by 2035. The expansion of urban impervious surface (UIS) is one of the prominent characteristics of urbanization, which affects the material circulation of the urban ecosystem, potentially leading to a series of ecological problems, such as increased surface runoff [2], enhanced heat island effect [3], decreased urban environmental quality [4], to list a few. UIS, considered as an essential indicator for meaturing urban ecology, mainly includes buildings, roads, parking lots, and other land covers where water cannot penetrate into the underground. Recently, one of the sustainable development goals of the United Nations 2030 Agenda for Sustainable Development is to build inclusive, safe, resilient, and sustainable cities and human settlements. The expansion pattern of UIS is a crucial part of this development strategy, and understanding the spatial and temporal distribution of UIS can benefits the construction of sponge cities and promotes the sustainable development of cities [5]. Therefore, monitoring, extracting, and mapping UIS are of great importance.

Remote sensing technology has become an important tool for extracting UIS due to its low cost and efficiency. According to some previous literature reviews [6], [7], UIS extraction methods based on remote sensing can be divided into the following four categories: spectral mixing analysis, image classification methods, index methods, and multisource data fusion methods. However, most of these methods used optical remote sensing data as the data source, such as moderate resolution imaging spectroradiometer data with a resolution of 500 m [8], nighttime light data with a resolution of 1 km [9], Landsat data with a resolution of 30 m [10], and Sentinel-2 data with a resolution of 10 m [11]. Although optical remote sensing provides direct knowledge on impervious surfaces, the phenomenon of "the same thing with the different spectrum, the same spectrum with foreign bodies" stands out and cannot be ignored. At the same time, optical remote sensing usually owns data quality issues that include cloud contamination and rain/snow obstacles, resulting in less available data. For example, Landsat could theoretically provide data with a spatial resolution of 30 m and a revisit cycle of eight days. However, due to the influence of weather, light, and other limitations, the actual effective observation frequency of Landsat ranges from biweekly to bimonthly (even less in certain occasions), falling short to meet the requirements of

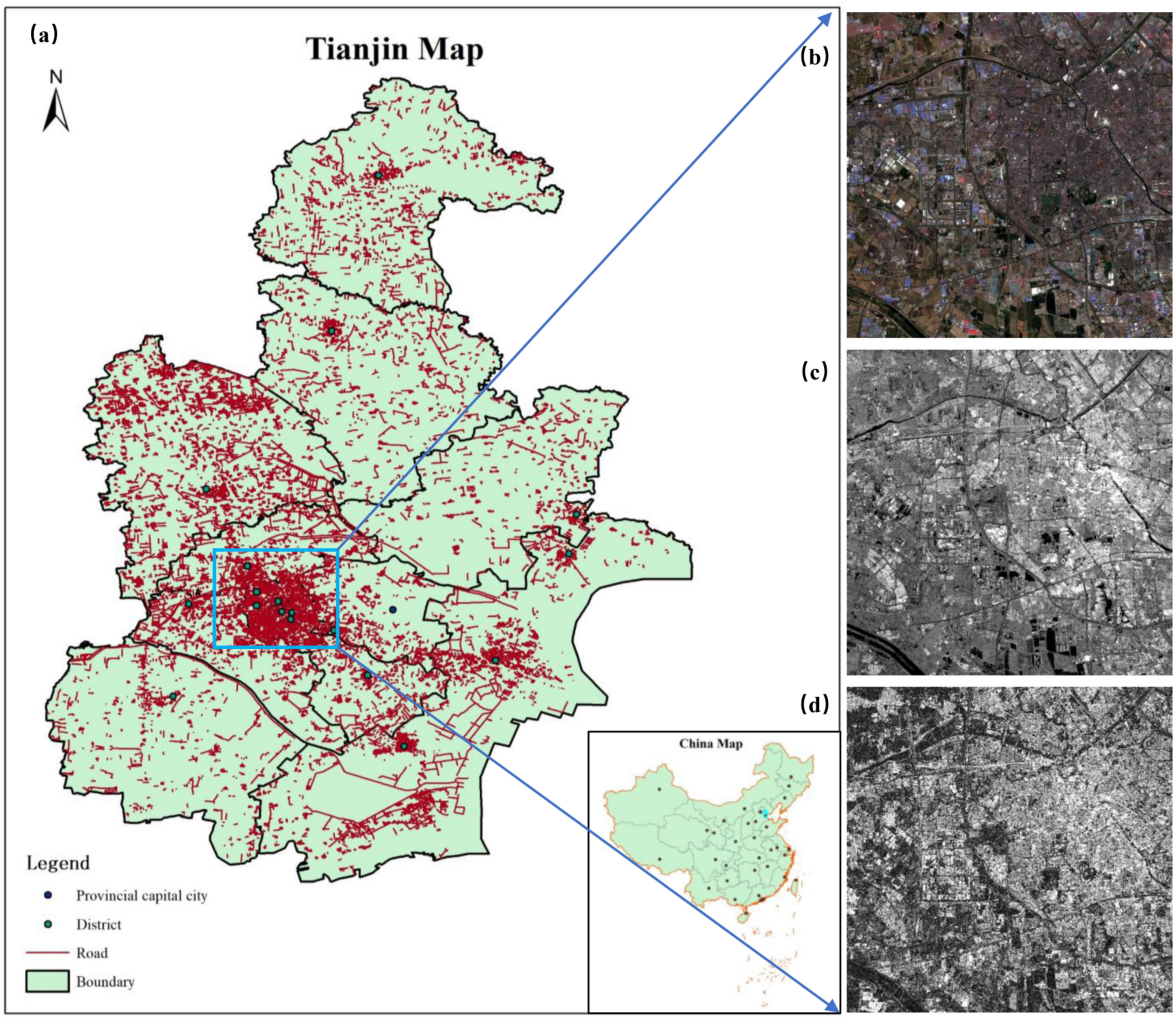

Fig. 1. Geographical location of the study area. (a) Map of Tianjin; (b)–(d) are Sentinel-2 A (true color), VH backscattering, and VH coherence images covering the study area, respectively.

UIS continuous monitoring [12]. All of the aforementioned limitations of optical remote sensing led us to explore new data sources for extracting UIS.

To address the limitations of optical remote sensing imagery, active remote sensing data, such as light detection and ranging and synthetic aperture radar (SAR), especially SAR, have been used to extract UIS. Different from optical sensors, SAR, as an active imaging system, has all-weather and day-and-night imaging capability due to its long wavelength, making it as an ideal data source that can complement optical remote sensing. For example, Zhang *et al.* [13] extracted UIS by fusing texture features of optical and SAR images, and achieved better results than using optical data alone. Then, in order to reduce the influence of shadows on Sentinel-2 image on the extraction accuracy of UIS, Sun *et al.* [14] fused the polarization features of Sentinel-1 and the multispectral features of Sentinel-2, and proposed a hierarchical UIS extraction framework. And with the open source of Sentinel-1 data, SAR data has gradually become another important data source for UIS extraction, which has been verified in large-scale UIS extraction [1], [15]. Backscattering and coherence features are two main features of SAR images. However, the existing researches on UIS extraction based on SAR image mostly focus on the fusion of optical and SAR images, but the capability of SAR technology, by itself, in UIS extraction has not been thoroughly investigated. Besides, such a data fusion is a complex process that involves strict registration between images and manual design of fusion rules and choice of fusion levels, which brings great uncertainty to UIS extraction [13], [16]–[18]. Recently, some scholars have tried to use the coherence features of SAR images to classify land covers and achieved satisfactory results [19], [20], which provides inspiration for this study to extract UIS by using coherence features.

Therefore, this study explored the potential of UIS extraction using seasonal time series dual polarized SAR backscattering and coherence images. Two object-based classifiers were involved in the UIS extraction process. Specifically, we first segmented multitemporal Sentinel-2 multispectral images to delineate meaningful objects to suppress speckle in SAR images. To extract UIS, we used time series Sentinel-1B backscattering and coherence images with VH and VV polarization from different seasons through object-based K-means (OB-K-means)

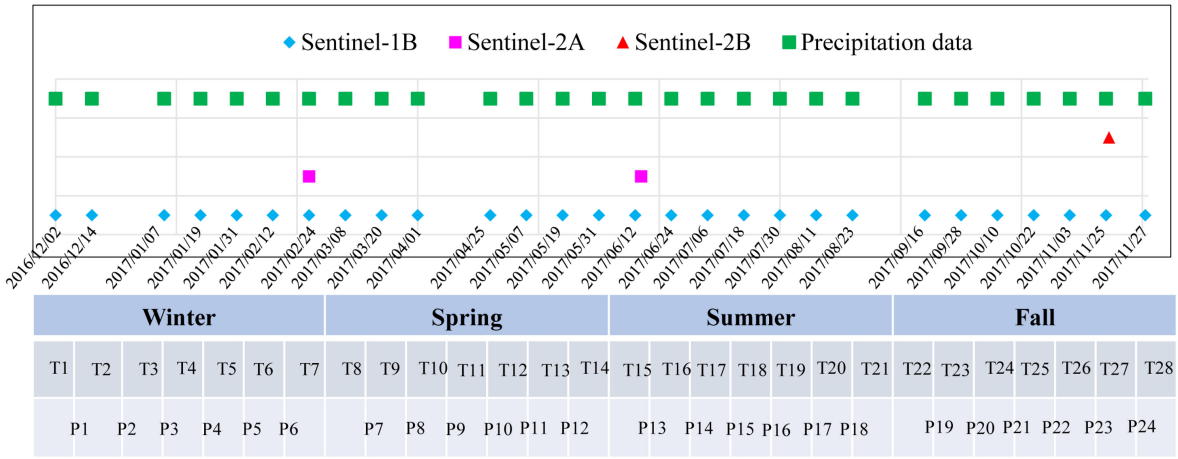

Fig. 2. Temporal coverage of data used in this study. T1–T28 represents the number of Sentinel-1 images obtained, and P1–P24 represents the number of InSAR pairs.

clustering algorithm based on dynamic time warping (DTW) distance and object-based random forest (OB-RF) algorithm, respectively. We further compared the results with the corresponding pixel-based classifiers. Finally, we analyzed the effects of season, polarization, and precipitation on UIS extraction using SAR images. To the best of authors' knowledge, this study marks the first to analyze the seasonal effects of SAR backscattering and coherence images on UIS extraction, providing a filling scheme for the data blind spots that existed in continuous monitoring of UIS in cloudy and rainy regions.

II. Study Area and Dataset

A. Study Area

In this study, we selected an area covering some developed districts located in Tianjin, including Nankai, Hexi, and Heping, as our study area [as shown in the rectangular area in Fig. 1(a)]. The selected area is with complete infrastructure and stable land covers. Tianjin is located at 116°43′ E–118°04′ E, 38°34′ N–40°15′ N, and its city center is located at 117°10′ E, 39°10′ N. Adjacent to Beijing, the capital of China, Tianjin is the largest industrial and commercial city in northern China. Thanks to its advantageous geographical location, Tianjin has seen rapid development in the past decades. Tianjin belongs to a temperate monsoon climate with four distinct seasons: Winter: December to February; Spring: March to May; Summer: June to August; Fall: September to November. The average annual precipitation of Tianjin is between 360 and 970 mm. Therefore, we chose Tianjin as our study area and explored the use of seasonal time series SAR backscattering and coherence images to extract its UIS.

B. Data Collection and Preprocessing

The data used in this study included daily precipitation data, and Sentinel-1 and Sentinel-2 images covering the study area of Tianjin. Their specific acquisition dates are shown in Fig. 2. Sentinel-1 and Sentinel-2 data were downloaded freely from the European Space Agency's, and the precipitation data were obtained by ground meteorological stations. In this study, three cloudless Sentinel-2 L1C images in different seasons were selected, which contain four bands of B (Band 2), G (Band 3), R (Band 4), and NIR (Band 8), with a spatial resolution of 10 m. Then, we used sen2cor plugin v2.8.0 available on the sentinel application platform (SNAP) v8.0 to conduct atmospheric correction on Sentinel-2 L1C data and obtained L2A data.

To estimate coherence, we acquired Level-1 Sentinel-1B single look complex (SLC) format data under the interferometric wide swath mode. A total of 28 SLC images were finally used, with 7 for each season. The backscattering and coherence information of Sentinel-1B were extracted through SNAP. The main preprocessing steps of extracting backscattering from SLC data included thermal noise removal, calibration, TOPSAR deburst, multilook, speckle filter, and terrain correction. Among them, the Refned Lee filter is used for speckle filtering. And to estimate coherence from SLC data, the main preprocessing steps included Sentinel-1 TOPS split, orbit correction, coregistration, deburst, coherence estimation, multilook, and terrain correction. In addition, we used the ENVI 5.3 software to register Sentinel-1 and Sentinel-2 data to the same geo-reference system of the Universal Transverse Mercator projection (Zone 50 N) and Datum WGS84. The root mean square error for registration was less than one pixel. The final spatial resolution of the images used in this study was 10 m.

III. Methodology

This section mainly described the overall workflow of this study (Fig. 3) in detail, which includes the following steps:

1) data preprocessing and generating time series SAR backscattering and coherence images in different seasons;
2) time series analysis;
3) multiresolution segmentation for multitemporal Sentinel-2 images;
4) extracting seasonal UIS using OB-K-means and OB-RF algorithms and assessing their accuracies;
5) investigating the seasonal, polarization, and precipitation effects on UIS extraction using SAR images.

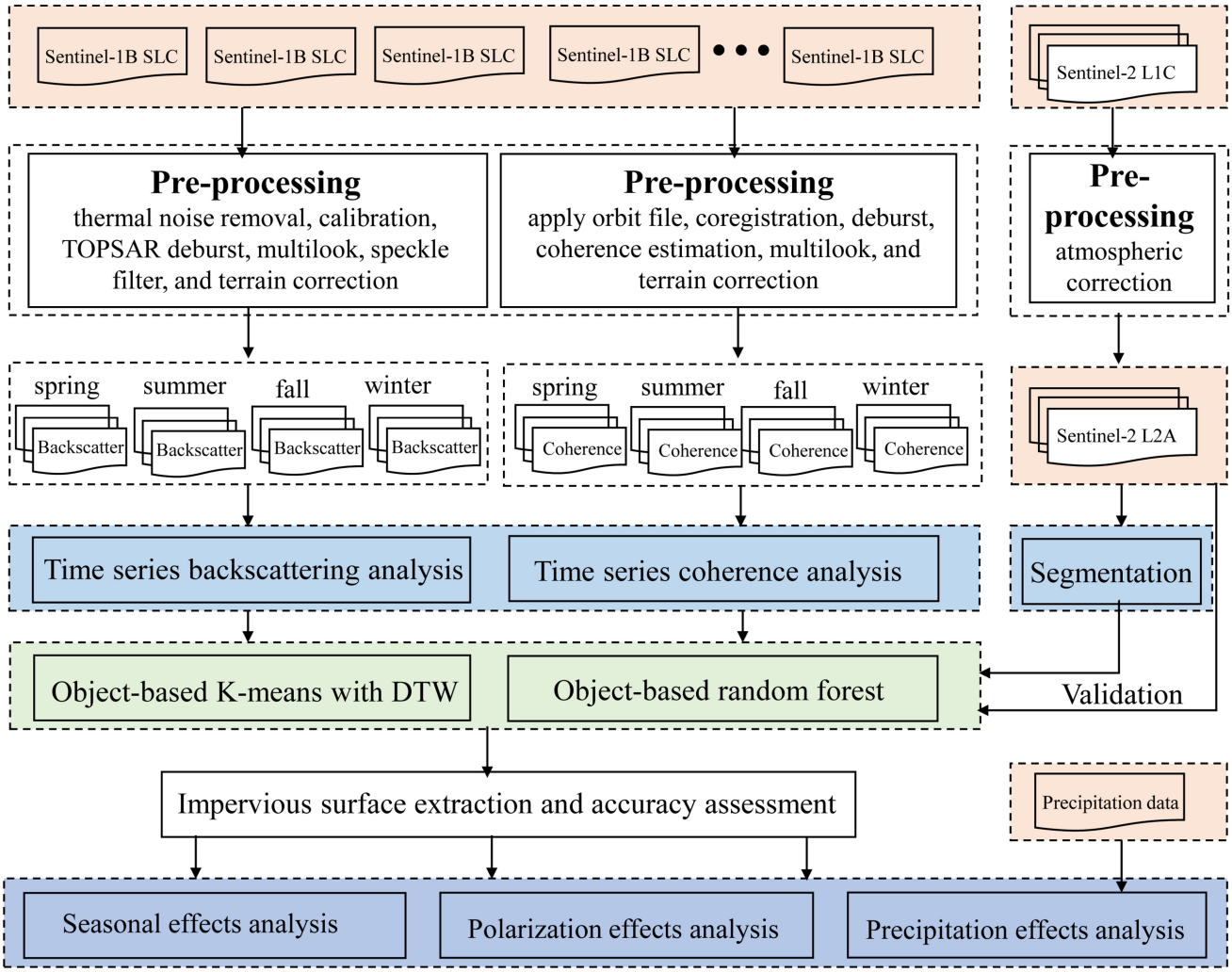

Fig. 3. Overall workflow of this study.

A. *Coherence Image Generation*

Coherence image, mainly used to guide phase unwrapping, is an intermediate product of interferometric SAR (InSAR) processing. The coherence directly reflects the mechanical stability of ground targets during the acquisition time intervals of the master and slave images [21], and it is negatively correlated with the randomness of the scatterers between the two SAR images. Different ground objects have different coherence, which is the theoretical basis of involving coherence images in UIS extracting. Coherence images have been used in various fields, such as land cover classification [22], flood mapping [23], and peat extraction [24], to list a few. Before estimating the coherence, it is necessary to register two SLC images that covered the same area. Further, the coherence between two coregistered SLC images can be estimated using the following formula:

$$\gamma = \frac{\left|\sum S_1(x)S_2(x)^*\right|}{\sqrt{\sum |S_1(x)|^2 \sum |S_2(x)|^2}} \tag{1}$$

where γ is the coherence value that ranges from 0 to 1. When $\gamma = 0$, it means completely incoherent; when $\gamma = 1$, it means completely coherent. S_1 and S_2 are the two coregistered SLC images, respectively. $*$ represents the complex conjugation. In this study, the window size for estimating the coherence is set to the default values of SNAP software, which is 10 in the range direction and 1 in the azimuth direction. To suppress the speckle in the coherence image, we use the mean filter to post process the coherence image, and the size of the filtering window is 3×3. In the future, we can consider using the time series SAR data despeckling toolbox developed in the literature [25] for better despeckling.

B. *Multiresolution Image Segmentation*

Due to the effect of speckle and the low distinguishability of ground objects, SAR data cannot provide sufficient detail [26]. To address this issue, we implemented image segmentation to generate homogeneous regions with the aid of Sentinel-2 image, aiming to suppress the effect of speckle in SAR image on UIS extraction. Given the seasonal effects, multitemporal Sentinel-2 images were used as input in the segmentation process. Due to the multiscale nature of remote sensing images,

TABLE I
DIFFERENT UIS EXTRACTION TESTS EMPLOYED IN THIS STUDY

No.	SAR features				Seasons			
	VH backscattering	VV backscattering	VH coherence	VV coherence	Spring	Summer	Fall	Winter
1	✓				✓			
2	✓					✓		
3	✓						✓	
4	✓							✓
5		✓			✓			
6		✓				✓		
7		✓					✓	
8		✓						✓
9			✓		✓			
10			✓			✓		
11			✓				✓	
12			✓					✓
13				✓	✓			
14				✓		✓		
15				✓			✓	
16				✓				✓

it is difficult to obtain satisfactory segmentation results using a single-scale segmentation algorithm. Therefore, multiresolution segmentation, a method based on the minimum heterogeneity under the constraint of the segmentation scale [27], was used in this study. After setting the appropriate segmentation scale, the heterogeneity after merging with adjacent pixels is calculated from a random pixel in the target image and compared with the segmentation scale. If the heterogeneity is less than the square of the segmentation scale, the adjacent pixels are merged. Otherwise, the segmentation process is ended. The heterogeneity of the image can be estimated using the following formula:

$$f = w \bullet h_{\text{color}} + (1 - w) \bullet h_{\text{shape}} \tag{2}$$

where h_{color} and h_{shape} indicate the spectral and shape heterogeneity, respectively. Their specific calculation formulas can be found in reference [28]. w is the weight that ranges from 0 to 1. More information on multiresolution segmentation can be found in the literature [27].

In this study, we conducted multiresolution segmentation using eCognition developer software. According to (2), scale, shape, and compactness are three key parameters of the multiresolution segmentation algorithm. Unfortunately, there is no common standards nor widely accepted approaches to determine the optimal segmentation parameters. The existing efforts tend to determine these parameters via the trial-and-error approach. Through multiple experiments and comparisons, we set the parameters of scale, shape, and compactness as 30, 0.1, and 0.5, respectively. Besides, to further avoid oversegmentation, spectral difference segmentation is carried out on the basis of multiresolution segmentation.

C. UIS Extraction

In this study, we implemented two object-based algorithms, i.e., OB-K-means and OB-RF, to extract UIS. We further compared them with their corresponding pixel-based methods, namely PB-K-means and PB-RF. Table I lists the different UIS extraction tests employed in this study.

1) K-Means Algorithm Based on DTW Distance: As a popular unsupervised classification algorithm, the basic steps of the K-means algorithm include the following:

1) determining the number of clusters (K) to be divided (number of ground objects categories);
2) selecting K pixels randomly from the image as the initial clustering center;
3) calculating the distance between the remaining pixels and the initial clustering center, and classifying each pixel into the category corresponding to the nearest clustering center;
4) recalculating the center of new classes. When the clustering centers remain unchanged for two consecutive iterations, the iteration ends.

Because we are concerned with UIS and pervious surface (NIS), the K is set to 2 in this study. In the K-means algorithm, the Euclidean distance is usually used as the clustering criterion. However, such distance measurement is not applicable to time series data. Comparing to Euclidean distance, the DTW distance can overcome the problem of scale displacement and the matching of unequal long time series data, thus leading to strong outlier resistance and better matching of similar features [29]. The larger the DTW distance, the greater the difference of time series data, and vice versa. Therefore, we selected the DTW distance as the clustering criterion of K-means in this study.

2) Random forest (RF): RF is an ensemble learning algorithm that has been widely used in various remote sensing applications (e.g., land cover classification [30], UIS extraction [31], aboveground biomass estimation [32]) and achieved satisfactory performances. In RF, the number of decision trees to be generated and the number of variables to be selected and tested for the best split when growing the trees (Mtry) are the two most important hyperparameters. In this study, we set them to 20 and 5 empirically, and apply them to all test cases employed in this study. The seasonal time series SAR backscattering and coherence images were used as input in the RF classifier, and the UIS and NIS were the output. Detailed information on RF can be found in [33].

D. Extraction Accuracy Assessment

In this study, the accuracies of UIS extraction were evaluated by two most commonly used indicators based on confusion matrix, i.e., overall accuracy (OA) and Kappa coefficient. To train the RF model and evaluate UIS extraction accuracies,

TABLE II
SENTINEL-1 INSAR PAIRS USED IN THIS STUDY FOR CALCULATING THE COHERENCE OF FOUR SEASONS IN TIANJIN

Season	Pair	Master–Slave	B. prep. [m]	B. temp. [Days]	Season	Pair	Master–Slave	B. prep. [m]	B. temp. [Days]
Winter	P1	2016/12/02–12/14	−19.19	−12	Spring	P7	2017/03/08–03/20	−50.84	−12
	P2	2016/12/14–2017/1/7	−113.95	−24		P8	2017/03/20–04/01	−42.78	−12
	P3	2017/01/07–01/19	−54.72	−12		P9	2017/04/01–04/25	−113.86	−24
	P4	2017/01/19–01/31	−25.49	−12		P10	2017/04/25–05/07	−12.29	−12
	P5	2017/01/31–02/12	−133.15	−12		P11	2017/05/07–05/19	−53.47	−12
	P6	2017/02/12–02/24	−33.19	−12		P12	2017/05/19–05/31	−158.73	−12
Season	Pair	Master–Slave	B. prep. [m]	B. temp. [Days]	Season	Pair	Master–Slave	B. prep. [m]	B. temp. [Days]
Summer	P13	2017/06/12–06/24	−12.08	−12	Fall	P19	2017/09/16–09/28	−54.63	−12
	P14	2017/06/24–07/06	−38.96	−12		P20	2017/09/28–10/10	−18.83	−12
	P15	2017/07/06–07/18	13.59	−12		P21	2017/10/10–10/22	−65.38	−12
	P16	2017/07/18–07/30	−6.11	−12		P22	2017/10/22–11/03	−32.89	−12
	P17	2017/07/30–08/11	−2.09	−12		P23	2017/11/03–11/15	−45.94	−12
	P18	2017/08/11–08/23	−35.89	−12		P24	2017/11/15–11/28	−55.7	−12

we randomly selected samples that were uniformly distributed throughout the study area through visual interpretation with the aid of high-resolution Google Earth images. A total of 2013 training samples (943 for UIS and 1072 for NIS) and 1373 validation samples (604 for UIS and 769 for NIS) were finally selected.

IV. EXPERIMENTAL RESULTS

A. Time Series Analysis of SAR Backscattering and Coherence

Due to the existence of disturbance, such as soil moisture, surface roughness, and speckle, uncertainty is likely to be introduced in the extraction of UIS using a single-temporal SAR image, potentially leading to low extraction accuracy. Thus, we decided to take advantage of time series SAR data. Before running all UIS extraction tests, we first analyzed the temporal patterns of UIS and NIS in SAR backscattering and coherence, which were rarely done in the previous studies. Time series backscattering and coherence images were generated according to the preprocessing steps described in Section II-B. Table II shows the dates of the different InSAR pairs in four seasons in Tianjin. Thanks to Sentinel's precise orbit control, the spatial baseline was smaller than the limit spatial baseline, so reliable coherence can be obtained. In consideration of the effect of temporal decorrelation, the temporal baseline we chose was mostly 12 days. Fig. 4 shows the time series box maps of SAR backscattering and coherence of UIS and NIS. In the box chart, the black line represents the average value of SAR backscattering and coherence features, and the box represents the main concentration range of the values. From this figure, some interesting findings can be noted, as follows.

1) The SAR backscattering and coherence of UIS are stable with relatively high values. The VH and VV backscattering of UIS fluctuate around -15 dB and -6 dB, respectively. The VH coherence fluctuates between 0.5 and 0.6, and the VV coherence fluctuates between 0.6 and 0.7.
2) The backscattering and coherence of NIS notably fluctuate under the influence of seasons. The fluctuation is intense in summer, which may be caused by summer precipitation (detailed discussions can be found in Section V-C).
3) The backscattering and coherence of UIS are considerably stronger than that of NIS. However, due to the fluctuation of NIS over time, there is uncertainty in the separability between UIS and NIS, which can affect the accuracy of extracting UIS using single-temporal SAR image. This is why we used time series SAR data in this study.
4) The differences in VH and VV polarization of UIS also affect its separability with NIS.

The abovementioned results indicate that it is feasible to use SAR backscattering and coherence to extract UIS. The extraction results are dependent on the polarization, seasons, and other factors, which reflects the significance of this study. To quantitatively compare the extraction ability of UIS using single-temporal and time series SAR data, we selected 50 UIS samples and 50 NIS samples from spring SAR images and calculated the single-temporal and time series features distance to measure the separability of UIS and NIS. Fig. 5 shows the calculated results with different SAR features. From Fig. 5, the distances of the time series feature between UIS and NIS are considerably higher than that of the single-temporal features. We also notice that the single-temporal feature distances of some samples are very small. These results indicate that compared with single-temporal SAR data, time series SAR data can improve the distinction between UIS and NIS, leading to improve UIS extraction accuracy, which again shows the rationality and necessity of using time series SAR data to extract UIS.

B. Impervious Surface Extraction Results

In order to illustrate the effectiveness of the object-based classification algorithms, i.e., OB-K-means and OB-RF, we took their corresponding pixel-based algorithms, PB-K-means and PB-RF, as the comparison algorithms in this study. Since the UIS distribution of each season in the study area was similar visually, we took spring as an example to show the UIS extraction results in this section. The analysis of seasonal effects was shown in the following sections.

Figs. 6 and 7 show the UIS extraction results using K-means and RF algorithms, respectively. Despite that the UIS distribution is similar overall, some differences can be found. For example, from Fig. 6, we notice that, compared with the extraction results of OB-K-means that of PB-K-means have a notable "salt-and-pepper" phenomenon. And this phenomenon can also be found in Fig. 7. These results indicate that the object-based classifier can effectively suppress speckle in SAR images. Besides, by comparing with the corresponding optical image, overestimation of UIS occurs in the results obtained by time series VV coherence image, as dry bare soils were misidentified as UIS (as shown in the elliptical regions of Fig. 6(d)). Similar

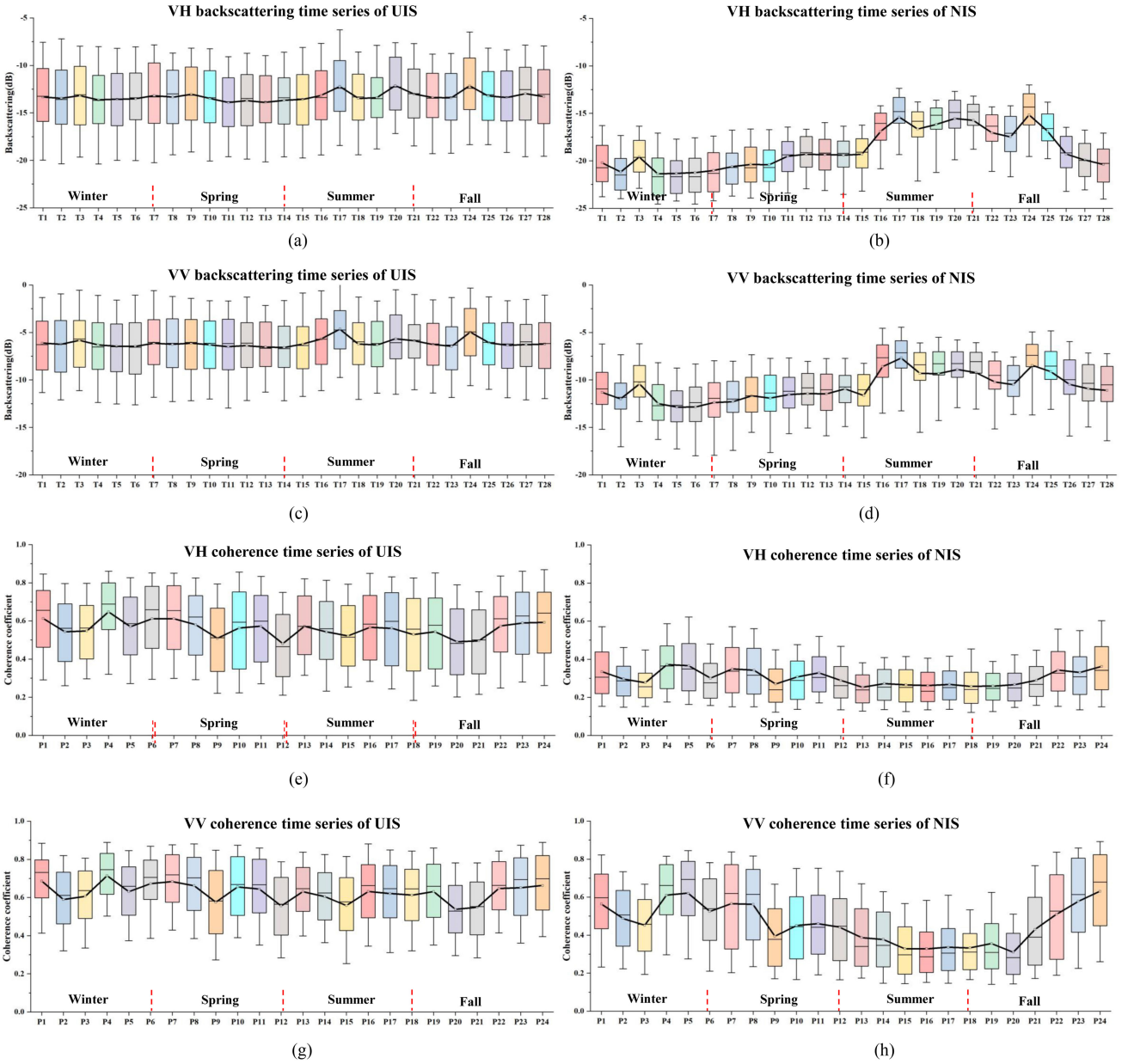

Fig. 4. Temporal patterns of SAR backscattering and coherence for UIS and NIS in the study area.

TABLE III
OA AND KAPPA COEFFICIENT OF UIS RESULTS EXTRACTED BY K-MEANS AND RF FROM SPRING TIME SERIES SAR IMAGES

Methods	VH backscattering		VV backscattering		VH coherence		VV coherence	
	OA (%)	Kappa	OA (%)	Kappa	OA (%)	Kappa	OA (%)	Kappa
PB-K-means	79.46	0.5646	79.90	0.5777	78.73	0.552	68.54	0.3613
OB-K-means	81.43	0.6093	79.02	0.5585	81.86	0.6195	72.83	0.4396
PB-RF	89.29	0.7815	82.96	0.6497	80.77	0.6023	77.49	0.5432
OB-RF	92.06	0.839	91.62	0.8285	91.19	0.8205	88.86	0.7727

issues can also be found in Fig. 7. To quantitatively assess the accuracies of UIS extraction and compare the results using different time series SAR features, Table III lists the OA and Kappa coefficients for the extraction results using K-means and RF with different SAR features, respectively. From Table III, we observe that the OA and Kappa coefficient obtained by the object-based methods are significantly higher than those obtained by the pixel-based methods, which is consistent with the above visualization results. In spring, the extraction accuracy of using time series coherence images is lower than that of using

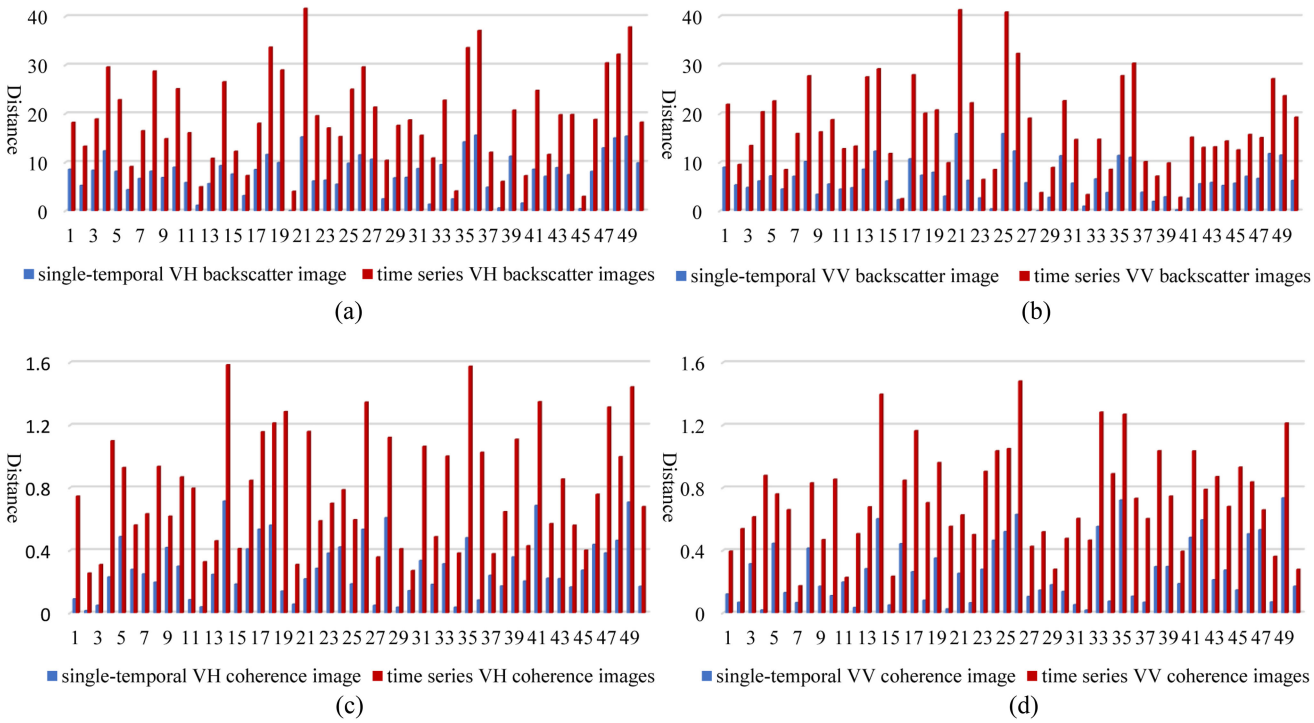

Fig. 5. Comparison of separability of UIS and NIS in time series SAR and single-temporal SAR data, respectively.

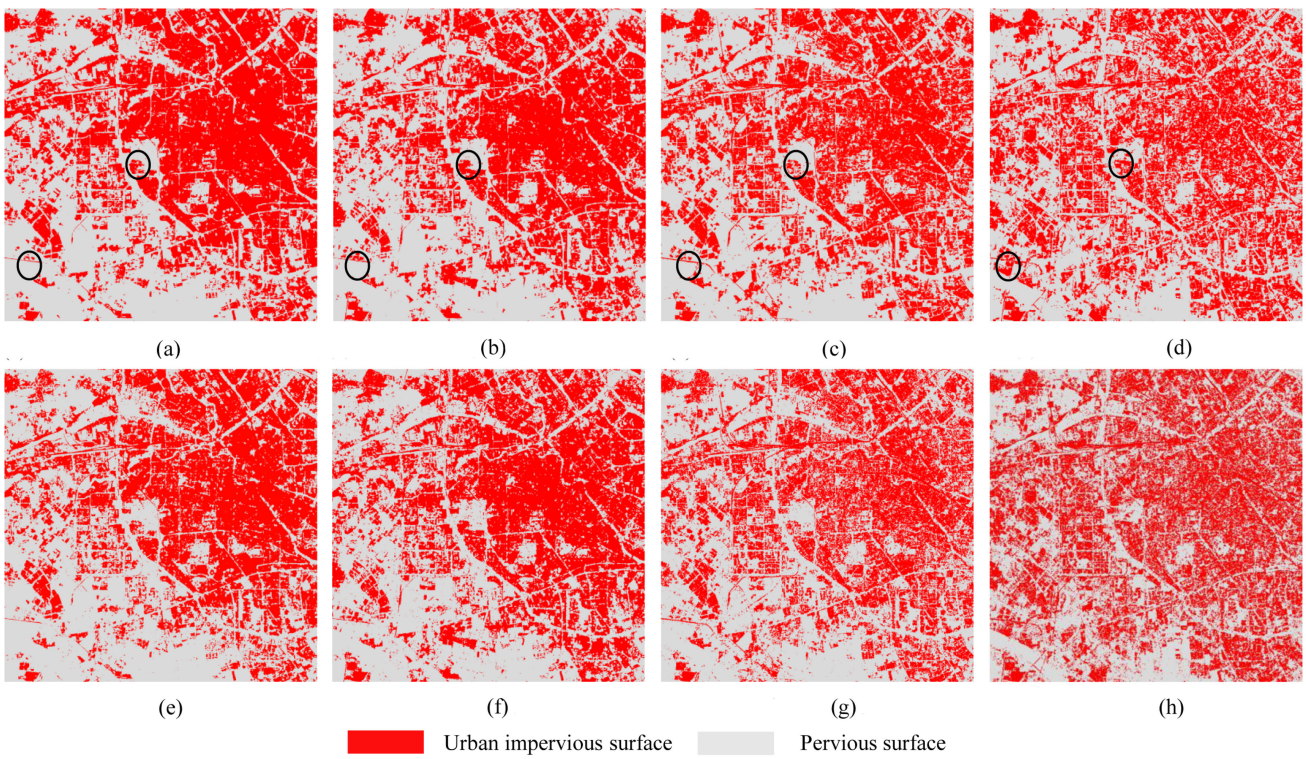

Fig. 6. UIS extraction results using PB-K-means and OB-K-means with different time series SAR features. (a) OB-K-means VH backscattering. (b) OB-K-means VV backscattering. (c) OB-K-means VH coherence. (d) OB-K-means VV coherence. (e) PB-K-means VH backscattering. (f) PB-K-means VV backscattering. (g) PB-K-means VH coherence. (h) PB-K-means VV coherence.

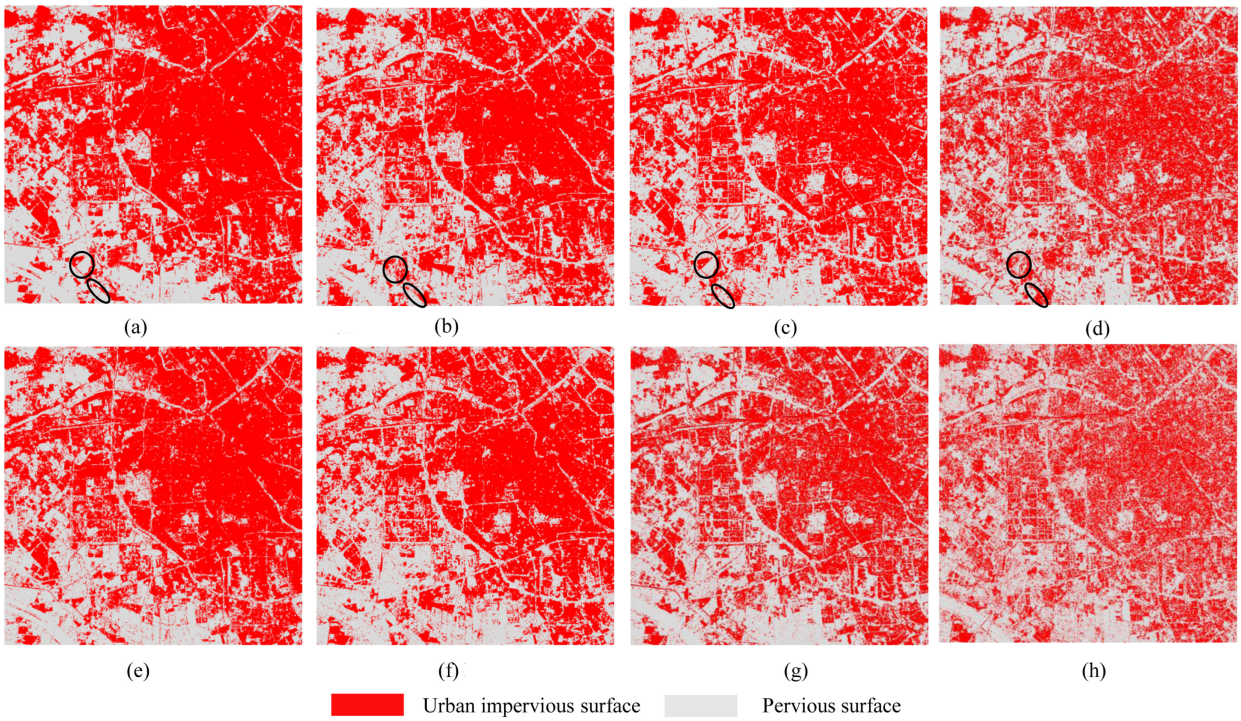

Fig. 7. UIS extraction results using PB-RF and OB-RF with different time series SAR features. (a) OB-RF VH backscattering. (b) OB-RF VV backscattering. (c) OB-RF VH coherence. (d) OB-RF VV coherence. (e) PB-RF VH backscattering. (f) PB-RF VV backscattering. (g) PB-RF VH coherence. (h) PB-RF VV coherence.

time series SAR backscattering, and the accuracy of results using the VV polarization coherence image is the lowest. Besides, the extraction accuracies obtained by the RF algorithm are considerably better than those obtained by K-means, and the PB-RF algorithm achieves a great performance, with OA up to 89% using VH backscattering, which indicates that the supervised machine learning classifier outperforms the unsupervised algorithm in the extraction of UIS. Therefore, the extraction of UIS using time series SAR data can be a feasible alternative when limited optical remote sensing data are available.

C. Comparison of Time Series SAR Backscattering and Coherence Images

The backscattering and coherence are the two most important features of SAR images, but their performance in UIS extraction has not been fully explored. Fig. 8 shows the comparison of the UIS extraction accuracy obtained by OB-K-means and OB-RF using time series SAR backscattering and coherence images in four seasons. From Fig. 8, we notice that for VH polarization, the accuracies of using time series backscattering are better than or close to that of using time series coherence images in spring, fall, and winter. However, in summer, the accuracies of using time series VH coherence images are higher than that of using time series VH backscattering images. This can be explained by Tianjin's precipitation pattern, where rainfall rarely occurs in spring, autumn, and winter, and less precipitation is observed, leading to stable SAR backscattering of UIS and NIS. Nevertheless, due to the influence of the precipitation in summer, the backscattering of the NIS fluctuates considerably, and the coherence of NIS decreases, resulting in decreased backscattering differences between NIS and UIS and increased coherence differences (more discussion can be found in Section V-C). For VV polarization, we notice that time series backscattering images perform better than time series coherence images in four seasons. The reason may be that VV polarization is sensitive to the changes of ground objects backscattering. The abovementioned findings suggest that for the purpose of extracting UIS, it is appropriate to use SAR backscattering in the dry season and coherence images in the nondry season, especially VH polarization.

V. Discussion

A. Seasonal Effects on UIS Extraction

Accurate UIS extraction is a challenging task due to the diversity of the vegetation phenology and climate. The seasonal effects on UIS extraction via optical remote sensing images have been investigated [34], while seasonal effects on UIS extraction via SAR images were relatively rare studied. Fig. 9 shows accuracies of UIS extraction obtained from different seasons using time series SAR backscattering and coherence images. From Fig. 9, we observe that different SAR features respond differently to different seasons. For VH and VV backscattering, the best results are obtained in spring, followed by winter. The worst result of VH backscattering is in summer, while that of VV backscattering is in fall. As shown in Fig. 9(c) and (g), the VH coherence achieves the best accuracy in summer and is relatively less affected by seasons, i.e., its UIS

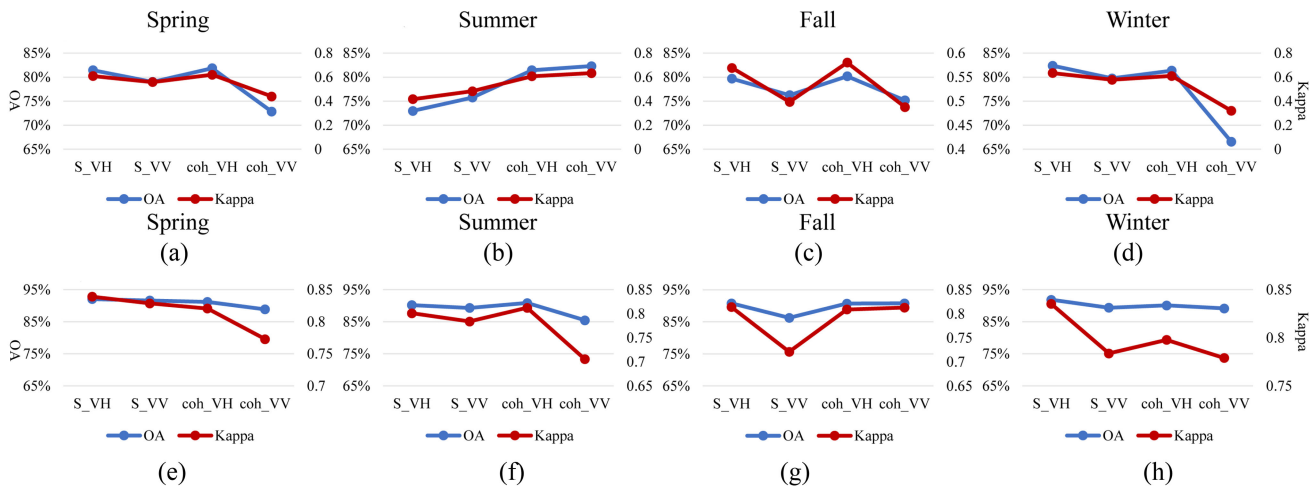

Fig. 8. Comparison of accuracies of UIS extraction obtained by time series SAR backscattering and coherence images. (a)–(d) Results obtained by OB-K-means, and (e)–(h) results obtained by OB-RF. The S_VH, S_VV, coh_VH, and coh_VV in the horizontal axis, respectively, represent VH backscattering, VV backscattering, VH coherence, and VV coherence.

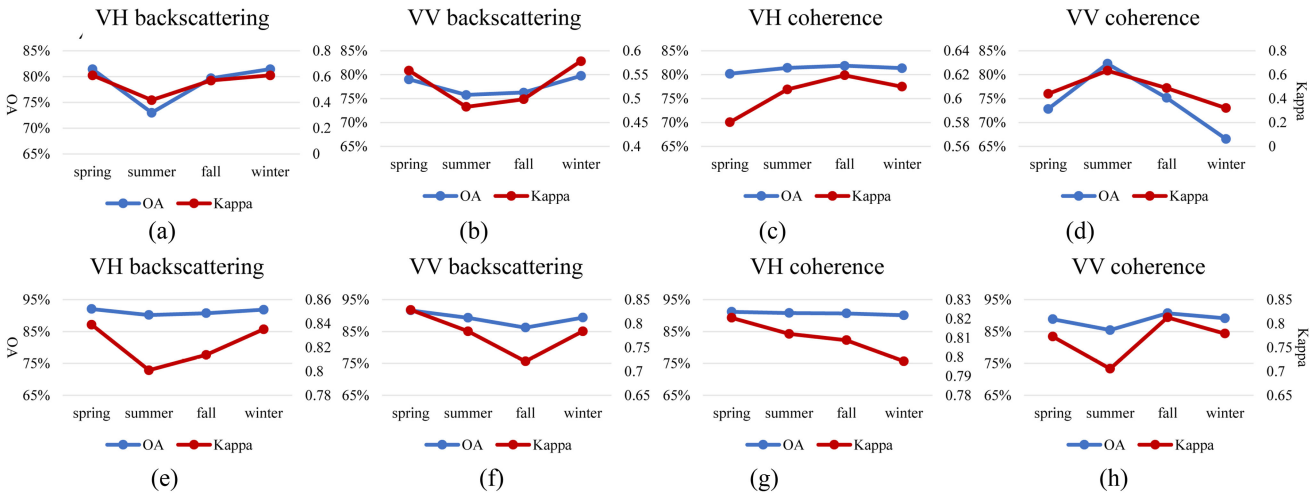

Fig. 9. Accuracies comparison of UIS extraction results obtained from different seasons using time series SAR backscattering and coherence images. (a)–(d) are the results obtained by OB-K-means, and (e)–(h) are the results obtained by OB-RF.

extraction accuracies are rather stable in four seasons. Compared with the VH coherence, the VV coherence is notably affected by seasons, with the largest performance disturbance occurring in winter [as shown in Fig. 9(d) and (h)]. Besides, compared with the RF algorithm, the K-means algorithm is more sensitive to seasonal changes. These results suggest that we should consider the seasonal effects and select the appropriate classifier and features accordingly during the UIS extraction process.

B. Polarization Effects on UIS Extraction

VH and VV are the two polarization modes of Sentinel-1 data used in this study, and their responses to impervious surfaces are different. Therefore, this section presents the performance disparity of VH and VV polarization in UIS extraction. Fig. 10 shows the OA of UIS extraction using VH and VV polarization features. From Fig. 10, we can find that the extraction accuracies obtained by VH polarization backscattering and coherence images are all higher than those obtained by VV polarization backscattering and coherence images in four seasons, regardless of the choice of classifiers. This finding is consistent with the previous studies [35]. The abovementioned comparison results indicate that VH polarization is more suitable than VV polarization in the extraction of UIS.

C. Precipitation Effects on Impervious Surface Extraction

The main sources of InSAR decoherence mainly include temporal decorrelation, spatial decorrelation, volume decorrelation, geometric decorrelation, and thermal noise from the antenna [8]. In this study, we only focused on temporal decorrelation caused by changes in the scatterers over time. The precipitation can

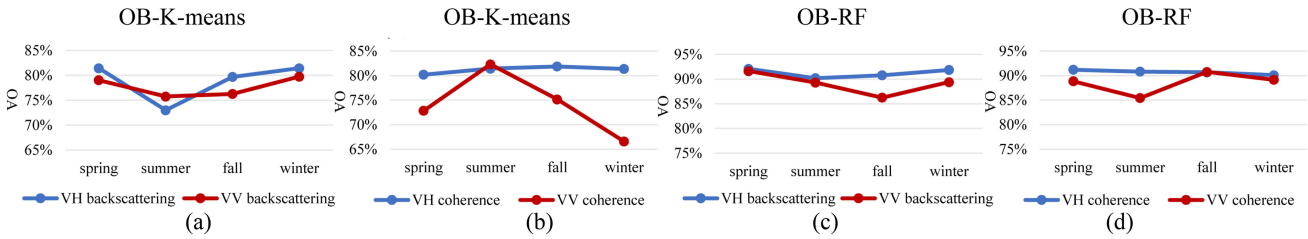

Fig. 10. Comparison of OA of UIS extraction performance with VH and VV polarization features.

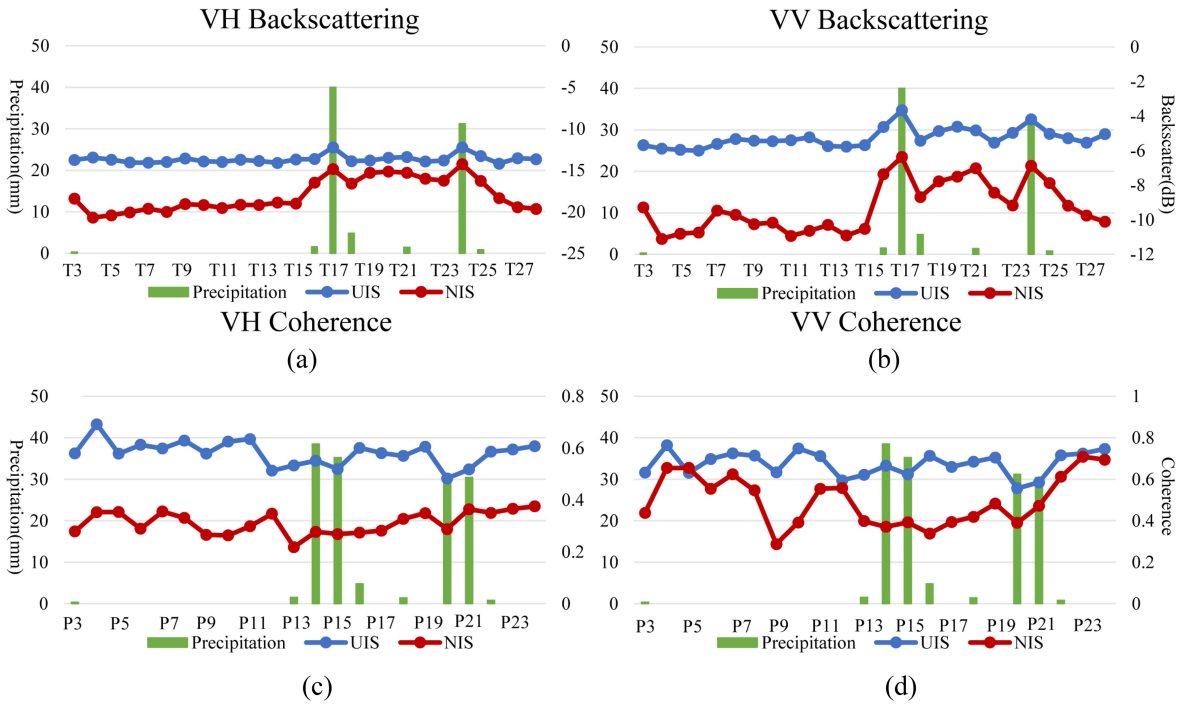

Fig. 11. Comparing the relationship between SAR backscattering and coherence and precipitation data in the study area in 2017. (a)–(d) VH backscattering, VV backscattering, VH coherence, and VV coherence, respectively.

TABLE IV
CORRELATION ANALYSIS BETWEEN PRECIPITATION AND SAR BACKSCATTERING AND COHERENCE OF UIS AND NIS

	VH backscattering		VV backscattering		VH coherence		VV coherence	
	Correlation	Significance	Correlation	Significance	Correlation	Significance	Correlation	Significance
IS	0.519	0.007	0.513	0.007	−0.633	0.002	−0.497	0.019
NIS	0.585	0.002	0.675	0.000	−0.362	0.098	−0.553	0.008

modify the permittivity of ground objects and further change the SAR backscattering, resulting in temporal decorrelation.

Therefore, we mainly analyze the influence of precipitation in the backscattering and coherence of UIS and NIS in this section. The daily precipitation data corresponding to Sentinel-1B data acquisition dates were obtained from the surface meteorological stations in Tianjin. To facilitate further analysis, a 2 km × 2 km buffer zone was established with a meteorological station (located in 117°04′12″ E, 30°04′48″ N) located in the study area as the center. A total of 100 UIS samples and 100 NIS samples were randomly and uniformly selected within the buffer zone to conduct correlation analysis of precipitation with SAR backscattering and coherence. Table IV shows the result of the correlation analysis. From Table IV, we notice that precipitation is positively correlated with the backscattering of ground objects but negatively correlated with the coherence of ground objects. Moreover, the correlation between the precipitation and NIS is stronger than that with UIS.

Fig. 11 shows the relationship between the precipitation and the mean backscattering and coherence of 100 NIS samples and 100 UIS samples. Note that, since only the precipitation data of 2017 were collected, the images acquired in December 2016 were removed from the analysis. From Fig. 11, we observe that in the case of rainfall, the SAR backscattering of NIS increases significantly and fluctuates considerably, while the SAR backscattering of UIS does not change much and remains

relatively stable, resulting in decreased coherence of NIS and the stable coherence of UIS with a high value. According to Fig. 11, we can conclude that in the dry season, the backscattering and coherence of NIS and UIS are stable, leading to great separability between NIS and UIS. However, in nondry season, due to the influence of precipitation, the backscattering of NIS is enhanced with weakened coherence, leading to the decreased separability between NIS and UIS in the backscattering and increased separability between NIS and UIS in the coherence, which can further explain the abovementioned experimental results in the Section IV. In addition, we also notice that the separability between NIS and UIS in VV coherence is better in the nondry season compared to the dry season. The abovementioned findings indicate that the influence of precipitation and other meteorological factors should be taken into consideration when using SAR images to extract UIS.

VI. Conclusion

UIS is an important indicator for measuring urban ecology, which is of great significance for alleviating urban diseases, such as heat island. However, affected by various factors, extracting UIS in an accurate manner is an important and challenging task. This study fully explored the utility and effectiveness of UIS extraction using seasonal time series SAR backscattering and coherence images, in order to find an alternative scheme of extracting UIS by optical remote sensing, and get rid of the restriction of weather on optical remote sensing. Two different approaches were investigated, i.e., OB-K-means and object-based RF classifiers. In addition, the seasonal, polarization, and precipitation effects on UIS extraction were also investigated. The results suggest that the extraction of UIS using time series SAR data can be a feasible alternative scheme when limited optical remote sensing data are available. The results also point to notable seasonal effects on UIS extraction using SAR image, and different SAR features tend to have different responses in different seasons. For coherence images, the UIS extraction accuracy in summer is the highest, while for backscattering, that in spring and winter is the highest. Compared with VV polarization, VH polarization is more suitable for UIS extraction. These findings of this study confirmed the utility and effectiveness of using time series SAR backscattering and coherence images in UIS extraction, providing an essential reference for UIS extraction in other places with a similar climate of the study area. We encourage more efforts to be made toward UIS extraction using SAR images and toward designing a filling scheme for the UIS extraction in a continuous manner, especially in cloudy and rainy areas.

References

[1] Y. Lin et al., "Incorporating synthetic aperture radar and optical images to investigate the annual dynamics of anthropogenic impervious surface at large scale," *Remote Sens. Environ.*, vol. 242, 2020, Art. no. 111757.

[2] Z. Shao et al., "Remote sensing monitoring of multi-scale watersheds impermeability for urban hydrological evaluation," *Remote Sens. Environ.*, vol. 232, 2020, Art. no. 111338.

[3] L. Li, Y. Zha, and J. Zhang, "Spatially non-stationary effect of underlying driving factors on surface urban heat islands in global major cities," *Int. J. Appl. Earth Observ. Geoinformation*, vol. 90, 2020, Art. no. 102131.

[4] M. A. Musse, D. A. Barona, and L. M. S. Rodriguez, "Urban environmental quality assessment using remote sensing and census data," *Int. J. Appl. Earth Observ. Geoinformation*, vol. 71, 2018, pp. 95–108.

[5] K. Anderson et al., "Earth observation in service of the 2030 agenda for sustainable development," *Geo-Spatial Inf. Sci.*, vol. 20, no. 2, pp. 77–96, 2017.

[6] Q. Weng, "Remote sensing of impervious surfaces in the urban areas: Requirements, methods, and trends," *Remote Sens. Environ.*, vol. 117, pp. 34–49, 2012.

[7] L. Zhang, Q. Weng, and Z. Shao, "An evaluation of monthly impervious surface dynamics by fusing Landsat and MODIS time series in the Pearl River Delta, China, from 2000 to 2015," *Remote Sens. Environ.*, vol. 201, pp. 99–114, 2017.

[8] A. Abdel-Hamid, O. Dubovyk, and K. Greve, "The potential of sentinel-1 InSAR coherence for grasslands monitoring in eastern cape, South Africa," *Int. J. Appl. Earth Observ. Geoinformation*, vol. 98, 2021, Art. no. 102306.

[9] J. Ou et al., "Evaluation of luojia 1-01 nighttime light imagery for impervious surface detection: A comparison with NPP-VIIRS nighttime light data," *Int. J. Appl. Earth Observ. Geoinformation*, vol. 81, pp. 1–12, 2019.

[10] L. Zhang, M. Zhang, and Y. Yao, "Mapping seasonal impervious surface dynamics in Wuhan urban agglomeration, China from 2000 to 2016," *Int. J. Appl. Earth Observ. Geoinformation*, vol. 70, pp. 51–61, 2018.

[11] D. Ienco et al., "Combining Sentinel-1 and Sentinel-2 satellite image time series for land cover mapping via a multi-source deep learning architecture," *ISPRS J. Photogrammetry Remote Sens.*, vol. 158, pp. 11–22, 2019.

[12] Z. Shao et al., "Deep learning-based fusion of Landsat-8 and Sentinel-2 images for a harmonized surface reflectance product," *Remote Sens. Environ.*, vol. 235, 2019, Art. no. 111425.

[13] Y. Zhang, H. Zhang, and H. Lin, "Improving the impervious surface estimation with combined use of optical and SAR remote sensing images," *Remote Sens. Environ.*, vol. 141, pp. 155–167, 2014.

[14] G. Sun et al., "Hierarchical fusion of optical and dual-polarized SAR on impervious surface mapping at city scale," *ISPRS J. Photogrammetry Remote Sens.*, vol. 184, pp. 264–278, 2022.

[15] Z. Sun et al., "Global 10-m impervious surface area mapping: A big earth data based extraction and updating approach," *Int. J. Appl. Earth Observ. Geoinformation*, vol. 109, 2022, Art. no. 102800.

[16] H. Guo et al., "Synergistic use of optical and PolSAR imagery for urban impervious surface estimation," *Photogrammetric Eng. Remote Sens.*, vol. 80, no. 1, pp. 91–102, 2014.

[17] H. Zhang et al., "A manifold learning approach to urban land cover classification with optical and radar data," *Landscape Urban Plan.*, vol. 172, pp. 11–24, 2018.

[18] Z. Shao, W. Wu, and S. Guo, "IHS-GTF: A fusion method for optical and synthetic aperture radar data," *Remote Sens.*, vol. 12, no. 17, 2020, Art. no. 2796.

[19] M. Jiang et al., "Delineation of built-up land change from SAR stack by analysing the coefficient of variation," *ISPRS J. Photogrammetry Remote Sens.*, vol. 169, pp. 93–108, 2020.

[20] T. Esch, M. Thiel, A. Schenk, A. Roth, A. Muller, and S. Dech, "Delineation of urban footprints from TerraSAR-X data by analyzing speckle characteristics and intensity information," *IEEE Trans. Geosci. Remote Sens.*, vol. 48 no. 2, pp. 905–916, Feb. 2010.

[21] H. Jin, G. Mountrakis, and S. V. Stehman, "Assessing integration of intensity, polarimetric scattering, interferometric coherence and spatial texture metrics in PALSAR-derived land cover classification," *ISPRS J. Photogrammetry Remote Sens.*, vol. 98, pp. 70–84, 2014.

[22] M. Jiang et al., "The potential of more accurate InSAR covariance matrix estimation for land cover mapping," *ISPRS J. Photogrammetry Remote Sens.*, vol. 126, pp. 120–128, 2017.

[23] Y. Li, S. Martinis, and M. Wieland, "Urban flood mapping with an active self-learning convolutional neural network based on TerraSAR-X intensity and interferometric coherence," *ISPRS J. Photogrammetry Remote Sens.*, vol. 152, pp. 178–191, 2019.

[24] T. Tampuu et al., "Detecting peat extraction related activity with multitemporal Sentinel-1 InSAR coherence time series," *Int. J. Appl. Earth Observ. Geoinformation*, vol. 98, 2021, Art. no. 102309.

[25] M. Jiang and A. M. Guarnieri, "Distributed scatterer interferometry with the refinement of spatiotemporal coherence," *IEEE Trans. Geosci. Remote Sens.*, vol. 58 no. 6, pp. 3977–3987, Jun. 2020.

[26] M. Mahdianpari et al., "Random forest wetland classification using ALOS-2 l-band, RADARSAT-2 c-band, and TerraSAR-X imagery," *ISPRS J. Photogrammetry Remote Sens.*, vol. 130, pp. 13–31, 2017.
[27] D. C. Duro, S. E. Franklin, and M. G. Dubé, "A comparison of pixel-based and object-based image analysis with selected machine learning algorithms for the classification of agricultural landscapes using SPOT-5 HRG imagery," *Remote Sens. Environ.*, vol. 118, pp. 259–272, 2012.
[28] L. Zheng and W. Huang, "Parameter optimization in multi-scale segmentation of high resolution remotely sensed image and its application in object-oriented classification," in *Proc. Int. Conf. Environ. Eng. Remote Sens.*, 2015, pp. 84–90.
[29] M. Belgiu and O. Csillik, "Sentinel-2 cropland mapping using pixel-based and object-based time-weighted dynamic time warping analysis," *Remote Sens. Environ.*, vol. 204, pp. 509–523, 2018.
[30] P. Du et al., "Random forest and rotation forest for fully polarized SAR image classification using polarimetric and spatial features," *ISPRS J. Photogrammetry Remote Sens.*, vol. 105, pp. 38–53, 2015.
[31] Z. Shao et al., "Mapping urban impervious surface by fusing optical and SAR data at the decision level," *Remote Sens.*, vol. 8, no. 11, 2016, Art. no. 945.
[32] Z. Shao, W. Wu, and D. Li, "Spatio-temporal-spectral observation model for urban remote sensing," *Geo-Spatial Inf. Sci.*, vol. 24, no. 3, pp. 372–386, 2021.
[33] L. Breiman, "Random forests," *Mach. Learn.*, vol. 45, no. 1, pp. 5–32, 2001.
[34] H. Zhang, Y. Zhang, and H. Lin, "Seasonal effects of impervious surface estimation in subtropical monsoon regions," *Int. J. Digit. Earth*, vol. 7 no. 9, pp. 746–760, 2014.
[35] W. Wu et al., "Extraction of impervious surface using Sentinel-1 A time-series coherence images with the aid of a Sentinel-2 A image," *Photogrammetric Eng. Remote Sens.*, vol. 87, no. 3, pp. 161–170, 2021.

Wenfu Wu received the master's degree in photogrammetry and remote sensing in 2019 from Wuhan University, Wuhan, China, where he is currently working toward the Ph.D. degree in photogrammetry and remote sensing.

His research interests include synthetic aperture radar (SAR) image despeckling, the fusion of optical and SAR images, and the applications of deep learning in remote sensing.

Zhenfeng Shao received the Ph.D. degree in photogrammetry and remote sensing from Wuhan University, Wuhan, China, in 2004. Since 2009, he has been a Full Professor with the State Key Laboratory of Information Engineering in Surveying, Mapping and Remote Sensing (LIESMARS), Wuhan University. He has authored or coauthored more than 50 peer-reviewed articles in international journals. His research interests include high-resolution image processing, pattern recognition, and urban remote sensing applications.

Dr. Shao was a recipient of the Talbert Abrams Award for the Best Paper in Image Matching from the American Society for Photogrammetry and Remote Sensing in 2014 and the New Century Excellent Talents in University from the Ministry of Education of China in 2012. Since 2019, he was an Associate Editor for the *Photogrammetric Engineering and Remote Sensing* (PE and RS) specializing in smart cities, photogrammetry, and change detection.

Jiahua Teng received the master's degree in photogrammetry and remote sensing from the China University of Mining and Technology, Beijing, China, in 2018.

He is currently an Engineer With the Ministry of Ecology and Environment Center for Satellite Application on Ecology and Environment, China. His research interest is the application of synthetic aperture radar (SAR) in ecological protection.

Xiao Huang received the B.S. degree in remote sensing science and technology from Wuhan University, Wuhan, China, in 2015, the master's degree in geographic information science and technology from the Georgia Institute of Technology, Atlanta, GA, USA, in 2016, and the Ph.D. degree in geography from the University of South Carolina, Columbia, SC, USA, in 2020.

He is currently an Assistant Professor with the Department of Geosciences, University of Arkansas, Fayetteville, AR, USA. His research interests cover GeoAI, deep learning, and human–environment interactions.

Xinwei Zhao received the master's degree in photogrammetry and remote sensing from the China University of Mining and Technology, Beijing, China, in 2018.

He is currently an Engineer with the China Centre for Resources Satellite Data and Application. His research interests include remote sensing monitoring of resources and environment.

Songjing Guo received the master's degree in surveying and mapping engineering in 2020 from the China University of Geosciences, Wuhan, China, where she is currently working toward the Ph.D. degree in spatial information detection.

Her research interests include ecological carrying capacity assessment and geological hazard detection using remote sensing technology.